Integrating Autofocus Techniques With Fast Factorized Back-Projection for High-Resolution Spotlight SAR Imaging

Lei Zhang, *Member, IEEE*, Hao-lin Li, Zhi-jun Qiao, *Member, IEEE*, Meng-dao Xing, *Member, IEEE*, and Zheng Bao, *Life Senior Member, IEEE*

***Abstract*—Back-projection (BP) is considered as an ideal methodology for the high-resolution synthetic aperture radar (SAR) imaging. However, applying conventional autofocus techniques to BP imagery requires a special consideration and is usually difficult to implement. In this letter, we present a scheme to compatibly blending a novel multiple aperture map drift (MAMD) algorithm with fast factorized back-projection (FFBP). Through an elaborate BP coordinate, we construct the Fourier transform relationship between FFBP sub-aperture (SA) images and the corresponding range-compressed phase history data. The phase error function is achieved by the MAMD within FFBP recursions, and well-focused imagery is obtained by phase correction on the range-compressed phase history data. The proposed scheme inherits the advantages of high precision and efficiency of the FFBP, and is suitable for high-resolution spotlight SAR imaging with raw data. Real data experiments guarantee the effectiveness of our proposed scheme.**

***Index Terms*—Autofocus, back-projection (BP), fast factorized back-projection (FFBP), multiple aperture map drift (MAMD), synthetic aperture radar (SAR).**

I. Introduction

BACK-projection (BP) has been accepted as an ideal approach for high-resolution spotlight synthetic aperture radar (SAR) imaging [1]–[3]. Rooted in the basic principle of wideband beam-forming, BP offers a number of advantages over the traditional SAR image formations, such as compensation of curve wave-front effect without geometric distortions or blurs, inherent accommodation of digital elevation map for topography and aperture-dependent motion compensation [4], [5]. However, the intensive computation burden of BP integrant prevents its applications from many operating scenarios. Many efforts have been devoted into accelerating the BP integrant, and the fast factorized back-projection (FFBP) is one of the most essential fast BP algorithms [2]. Running in a recursive manner, FFBP dramatically reduces the computation burden of the BP and is approximately equivalent to the efficiency of traditional fast Fourier transform based frequency-domain algorithms, such as range-Doppler and chirp-scaling algorithms.

Like the conventional BP algorithm, FFBP is inherently compatible with motion compensation by the precise measurements from the position systems, such as GPS and INS/IMU. However, it is only the case when the position precision is high up to the wavelength order, which is usually beyond the accuracy of some economic position systems. As a result, autofocus is a key element in high-resolution SAR imaging with FFBP. Without loss of generality, two factors should be accounted in autofocus techniques [4]. First, the blurs, caused by residual motion error, should only distribute along the azimuth direction in the range-compressed phase history data. Second, the Fourier transform between image and the corresponding range-compressed phase history data is a fundamental requirement in most autofocus methods, such as phase gradient autofocus (PGA) algorithm. Traditional frequency-domain imaging algorithms can naturally imply this property (such as polar format algorithm), or with cooperation with the de-ramping processing [6], [7]. However, this relationship is not clear in both BP and FFBP formation. In [4], it has been revealed that there exists an approximate Fourier transform relationship when the image is projected onto the polar coordinate. Selection of image coordinate is elementary in developing an autofocus scheme for BP and FFBP imagery.

In this letter, we propose an autofocus scheme associating with FFBP algorithm for high-resolution spotlight SAR imagery. Conventional FFBP represents sub-aperture (SA) images in the local polar coordinate (r, θ), and the BP integrant is implemented by coherently fusing SA images in a recursive manner. Herein, we map SA images onto a pseudo polar coordinate under the scheme of FFBP, namely, $(r, \sin\theta)$. Detailed mathematical derivation is presented to develop the analytic expression of impulse response function (IRF) of BP in the coordinate. Based on the IRF expression, the relationship of Fourier transform between SA image and the corresponding phase history are analyzed. A novel multiple aperture map drift algorithm is developed, which is integrated within the FFBP recursion. Precise phase error function is achieved recursively, and well-focused imagery is obtained after motion error correction. The proposed scheme inherits the advantages of high precision and efficiency of the FFBP, and is suitable for high-resolution spotlight SAR imaging.

Manuscript received January 6, 2013; revised March 5, 2013; accepted April 15, 2013. Date of publication July 19, 2013; date of current version October 10, 2013. This work was supported by the Fundamental Research Funds for the Central Universities under Grant K5051302001 and K5051302038, and the Natural Science Foundation of China under Grant 61222108.

L. Zhang, H. Li, M. Xing, and Z. Bao are with the National Lab of Radar Signal Processing, Xidian University, Xi'an 710071, China (e-mail: leizhang@xidian.edu.cn; lihaolin322@163.com; xmd@xidian.edu.cn; zhbao@xidian.edu.cn).

Z. Qiao is with the Department of Mathematics, University of Texas-Pan American, Edinburg, TX 78539-2999 USA (e-mail: qiao@utpa.edu).

Color versions of one or more of the figures in this paper are available online at http://ieeexplore.ieee.org.

Digital Object Identifier 10.1109/LGRS.2013.2258886

II. Impulse Response Function and Phase Error in BP Image

In this section, we introduce signal model and basic principle of BP integrant in the pseudo polar coordinate. Considering ideal case without motion error (the motion error case will be discussed in the next subsection), a SAR sensor moves along a straight-line flight track with constant velocity v generating a synthetic aperture with length L. During the signal acquisition, the radar beam center always illuminates the scene center. When the antenna phase center locates at $X = vt$ (where t denotes the slow time) along the x-axis, the instantaneous range from radar to a point with polar coordinate (r_p, θ_p) is given by

$$R(X; r_p, \theta_p) = \sqrt{r_p^2 + X^2 - 2r_p X \sin\theta_p}, \quad -\frac{L}{2} \le X < \frac{L}{2}. \tag{1}$$

Suppose the transmitted pulsed chirp signal is $s_t(\tau) = \mathrm{rect}(\tau/T) \cdot \exp[j2\pi(f_c\tau + \gamma\tau^2/2)]$, where γ is the chirp rate, T is the pulse duration width, and τ denotes the range fast-time. After down-conversion to the base-band, the received signal at the point X is given by

$$s(\tau, X) = \varepsilon_p \cdot \mathrm{rect}\left(\frac{\tau - \Delta t}{T}\right) \cdot \mathrm{rect}\left(\frac{X}{L}\right) \cdot \exp\left[j2\pi\left(-f_c\Delta t + \frac{\gamma(\tau - \Delta t)^2}{2}\right)\right] \tag{2}$$

where $\Delta t = 2R(X; r_p, \sin\theta_p)/c$ corresponds to the round-way time delay, c is the speed of light, and ε_p denotes the complex-valued reflectivity coefficient. Applying the matched-filtering in the range dimension, the range-compressed signal is expressed as follows:

$$s_{MF}(\tau, X) = \varepsilon_p \cdot \mathrm{sinc}\left[\gamma T(\tau - \Delta t)\right] \cdot \mathrm{rect}\left(\frac{X}{L}\right) \cdot \exp(-j2\pi f_c \Delta t). \tag{3}$$

In the following, we focus on the derivation of analytic expression of the Impulse Response Function in the pseudo polar coordinates with the BP processing. The IRF for the point (r_p, θ_p) in the pseudo polar coordinate can be obtained by calculating the expression on a local neighborhood around the grid near the point. For simplicity, let $k_p = \sin\theta_p$ and $k = \sin\theta$, namely, the azimuth axis of the pseudo polar coordinate is defined by the variable k. Therefore, the IRF with BP is given as follows:

$$M(r_p, k) = \int_{X\in L} s_{MF}\left(\tau = \frac{2R(X; r_p, k)}{c}, X\right) \cdot \exp\left(j4\pi\frac{R(X; r_p, k)}{\lambda}\right) dX. \tag{4}$$

The magnitude of IRF on grid (r_p, k) is achieved as a coherent summation of the range-compressed signal along the range history $R(X; r_p, k)$, thus (4) may be simplified as

$$M(r_p, k) = \int_{X\in L} \varepsilon_p \cdot \exp\left(-j4\pi\frac{\Delta R(X; r_p, k)}{\lambda}\right) dX. \tag{5}$$

To derive the analytic expression of IRF, the differential range between $R(X; r_p, k_p)$ and $R(X; r_p, k)$ is analyzed by second-order Taylor series expansion. Generally, in a local neighborhood around the target grid, higher order terms usually take a fraction of $\Delta R(X; r_p, k)$

$$\begin{aligned}\Delta R(X; r_p, k) &= R(X; r_p, k_p) - R(X; r_p, k) \\ &= \frac{2r_p \cdot X(k_p - k)}{\sqrt{r_p^2 + X^2 - 2r_pXk} + \sqrt{r_p^2 + X^2 - 2r_pXk_p}} \\ &\approx (k_p - k)\cdot X + \frac{\left(k_p^2 - k^2\right)}{2r_p}\cdot X^2. \end{aligned} \tag{6}$$

From the above approximation, one can see if the quadratic term is nominal enough, and the integrant in (5) can be rewritten as

$$\begin{aligned} M(r_p, k) &\approx \int_{X\in L} \varepsilon_p \cdot \exp\left(-j4\pi\frac{(k_p - k)\cdot X}{\lambda}\right) dX \\ &= \int_{X\in L} \varepsilon_p \cdot \exp\left(-j\cdot\frac{4\pi\Delta k}{\lambda}\cdot X\right) dX \end{aligned} \tag{7}$$

where $\Delta k = (k_p - k)$. In (7), the Fourier transform relationship between X and $2\Delta k/\lambda$ is developed to yield a Sinc expression of IRF. Moreover, $4\pi\Delta k/\lambda$ exactly corresponds to the definition of the azimuth wavenumber. Given a certain aperture length L, the magnitude of the quadratic term in (6) increases as Δk deviates from zero. In general, the vast majority of energy of IRF is intensively concentrated within a very small region around $k = k_p$, and the region size corresponds to the azimuth resolution. Taking the angle coordinate of the point into account, the azimuth resolution is given by following equation [8]

$$\delta k = \frac{\lambda}{2L}. \tag{8}$$

To analyze the effect from the quadratic term on the shape of IRF, let $k = k_p + \Delta k$, then the quadratic term in (6) corresponding to the neighboring region around $k = k_p$ is given by

$$\frac{\left(k_p^2 - k^2\right)}{2r_p}\cdot X^2 = \frac{\left[k_p^2 - (k_p + \Delta k)^2\right]}{2r_p}\cdot X^2 \approx -\frac{\Delta k\cdot k_p}{r_p}\cdot X^2. \tag{9}$$

Actually, the quadratic term in (9) induces a quadratic phase error (QPE), i.e.,

$$\mathrm{QPE} = 4\pi\frac{\Delta k \cdot k_p}{\lambda r_p}\cdot X^2. \tag{10}$$

The magnitude of QPE is directly proportional to Δk. When the magnitude of QPE is small enough, its effect on (5) can be neglected, such as QPE is constrained to do not exceed $\pi/8$. As the shape of IRF is determined by the magnitude within a limited range of $[k_p - \delta k, k_p + \delta k]$, if QPE is small enough at the boundary, then the QPE effect on IRF is nominal as well. Substituting $\Delta k = \delta k$ into (12) and constraining the value of QPE under $\pi/8$, we have

$$2\pi\frac{k_p}{L\cdot r_p}\cdot\left(\frac{L}{2}\right)^2 \le \frac{\pi}{16} \tag{11}$$

which implies $k_pL \le (r_p/8)$. This means when the effective aperture k_pL is shorter than an eighth of r_p, the approximation in (7) is precise to ensure a Fourier transform pair relationship between the BP image and its corresponding range-compressed phase data. Actually, the constraint is generally easy to satisfy in reality. For the sake of quantitatively understanding, let an X-band SAR work in the broadside mode for a target

with range 10 km, a synthetic aperture of 2.5 km, leading to an azimuth resolution up to 0.12 meter, can still satisfy the condition (11). Of course, in high-resolution ultra-wideband (UWB) SAR imaging, the approximation accuracy in (7) would degrade. Actually, the IRF of high-resolution UWB-SAR has deeply been investigated in [9], [10], whose shape is very different the Sinc expression. However, for the high frequency band SAR imaging, the assumption is usually precise enough to integrate the autofocus techniques with BP imaging.

III. Autofocus Processing Within FFBP

In last section, the Fourier transform pair relationship between BP image and its range-compressed phase history is established. FFBP is a fast implementation of BP at a price of controllable precision degradation, and thus the relationship holds for FFBP, which paves a way to develop autofocus scheme for FFBP. In this section, we first introduce FFBP, and then the integration of autofocus techniques and FFBP is investigated in detail.

FFBP recursively partitions the complete back-projection integral into sub-aperture (SA) image blending. The basic principle of FFBP lies in that, by a proper image coordinate selection, the grid of the coordinate can be very coarse without losing any information in the case of BP integral of a short sub-aperture. In each processing stage of FFBP, finer angular resolution is obtained by interpolating coarse resolution SA images along with the increased sub-aperture length. By a repeated recursion procedure, the grid of SA images thins, and the number of SA images decreases. Correspondingly, the sampling rate in azimuth is also promoted with the update of FFBP recursion until blending the whole aperture together. In the beginning stage of FFBP, the full-aperture is partitioned into a set of short sub-apertures, and each sub-aperture is integrated into an image in a local polar coordinates system with coarse azimuth resolution. Then, the neighboring two SA images are fused into one image corresponding to new local polar coordinates with finer angular resolution. For the gth recursion, we assume there are U_g SA images corresponding to U_g local coordinates. For the uth SA image, the corresponding sub-aperture length is defined by $D_u^{(g)}$ and the local coordinates are denoted by $(r_u^{(g)}, \theta_u^{(g)})$ with sub-aperture center $A_u^{(g)}$. For clarity, we always use superscript "(g)" to express the gth FFBP recursion and subscript "u" to denote the uth sub-aperture.

To avoid ambiguity in azimuth, the grid of the SA image is restricted by [2]

$$\Delta\left(\sin\theta_u^{(g)}\right) \le \frac{\lambda_{min}}{2D_u^{(g)}} \tag{12}$$

where λ_{min} is the minimum wavelength corresponding the transmitted waveform. In the $(g+1)$th recursion, two neighboring sub-apertures are blended to generate $U_g/2$ images with finer azimuth resolution. This processing is illustrated in Fig. 1. For detailed mathematics of FFBP, one can see [4]. FFBP dramatically decreases the computational burden of BP with slight precision degradation due to accumulation of interpolation error. In this sense, the IRF of FFBP is equivalent to that of BP. Replacing the local polar coordinates of original FFBP by the pseudo polar coordinate, for instance, $(r_u^{(g)}, \sin\theta_u^{(g)})$ stands for the uth SA image within the gth recursion, there is

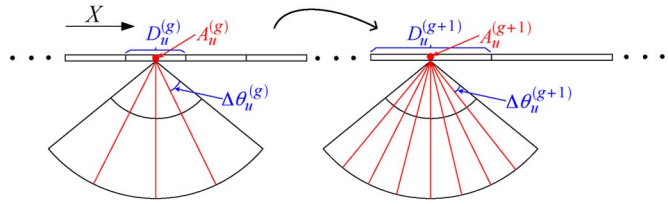

Fig. 1. Recursion of FFBP imaging.

also the relationship of Fourier transform pair between FFBP SA images and their range-compressed phase history. And the utilization of the pseudo polar coordinate also reduces computational burden of FFBP as some trigonometric calculation is avoided in the SA image fusion recursion.

In the following, we introduce the combination of current autofocus approaches with FFBP. At first, we define the azimuth interval of SA image as $\sin\theta_u^{(g)} \in [-(f\lambda/2v), f\lambda/2v]$, where $f = 2v\sin\Theta_u/\lambda$ corresponds to the definition of Doppler frequency and Θ_u determines the azimuth axis of SA image $[-\sin\Theta_u, \sin\Theta_u]$. In this sense, the pseudo polar coordinate corresponds to the Doppler domain in azimuth, which is equivalent to the azimuth domain of SPECAN imaging [11]. Assume the uth SA image within the gth recursion of FFBP is $h_u^{(g)}(r_u^{(g)}, \sin\theta_u^{(g)})$. According to the Fourier relationship derived in Section II, the corresponding range-compressed phase history is given by

$$h_u^{(g)}\left(r_u^{(g)}, t_u^{(g)}\right) = \int h_u^{(g)}\left(r_u^{(g)}, \sin\theta_u^{(g)}\right) \cdot \exp\left(j2\pi f_u^{(g)} t_u^{(g)}\right) df_u^{(g)} \tag{13}$$

where $f_u^{(g)} = (2\sin\theta_u^{(g)}/\lambda)$ corresponds to the Doppler frequency and $t_u^{(g)}$ is the counterpart time. Clearly, the time interval of $h_u^{(g)}(r_u^{(g)}, t_u^{(g)})$ is $1/(2f)$, and the central time corresponding to the origin of the pseudo polar coordinate is $A_u^{(g)}/v$, and v denotes the sensor velocity along track. The illustration of the geometry of $h_u^{(g)}(r_u^{(g)}, \sin\theta_u^{(g)})$ and $h_u^{(g)}(r_u^{(g)}, t_u^{(g)})$ is shown in Fig. 1.

In the following, we introduce motion error and autofocus processing. Supposing the major motion error is corrected in advance with high-precision measurements of navigation apparatus, such as GPS/IMU. The residual motion error is small without inducing migration through range cells, and it expresses itself as the just phase error. For each SA image $h_u^{(g)}(r_u^{(g)}, \sin\theta_u^{(g)})$, the deterministic range migration and phase history by the ideal data acquisition geometry are corrected precisely by the BP integral. As a result, the phase error is retained in $h_u^{(g)}(r_u^{(g)}, t_u^{(g)})$. First, the phase error is supposed to be spatial-invariant. The range-compressed phase history containing phase error can be expressed as follows:

$$h_u^{(g)}\left(r_u^{(g)}, t_u^{(g)}\right) = hi_u^{(g)}\left(r_u^{(g)}, t_u^{(g)}\right) \cdot \exp\left[-j\varphi\left(t_u^{(g)}\right)\right] \tag{14}$$

where $hi_u^{(g)}(r_u^{(g)}, t_u^{(g)})$ is the idea phase history, φ is the phase error induced by motion error $\Delta R(X = vt)$, and the phase error is supposed to be spatial-invariant. In general, the phase error can be approximated by Q-order polynomial as

$$\varphi(t_m) = -4\pi \cdot \Delta R(vt)/\lambda = \sum_{q=2}^{Q} a_q \cdot t^q \tag{15}$$

where a_q denotes the qth polynomial coefficient. Notably, the first-order term is neglected as it is usually compensated by Doppler centroid estimation [11], [12]. With respect to t, the second-order derivative of phase error corresponding to the instantaneous Doppler rate is expressed by the following equation:

$$\gamma(t_m) = \frac{\partial^2 \varphi(t)}{\partial t^2} = \sum_{q=2}^{Q} q \cdot (q-1) \cdot a_q \cdot t^{q-2}. \quad (16)$$

In the following, a novel multiple aperture map drift (MAMD) approach is integrated with FFBP to estimate the phase error. In the gth recursion of FFBP, U_g SA images are transformed into the range and time domain by inversed Fourier transform as (9) presents. The traditional map drift (MD) algorithm [8] is applied to each range-compressed phase history $h_u^{(g)}(r_u^{(g)}, t_u^{(g)})$ and a Doppler rate $\gamma_u^{(g)}$ is achieved. Therefore, the vector of instantaneous Doppler rate estimate can be written as

$$\zeta^{(g)} = \left[\gamma_1^{(g)} \quad \cdots \quad \gamma_{U_g-1}^{(g)} \quad \gamma_{U_g}^{(g)} \right]^T_{U_g \times 1} \quad (17)$$

where the symbol $[\cdot]^T$ denotes vector transpose. The instantaneous time of Doppler rate corresponds to the time center of sub-apertures. As a result, the instantaneous time vector corresponding to $\zeta^{(g)}$ is given by

$$\alpha^{(g)} = \left[A_1^{(g)}/v \quad \cdots \quad A_{U_g-1}^{(g)}/v \quad A_{U_g}^{(g)}/v \right]^T_{U_g \times 1}. \quad (18)$$

The polynomial coefficient can also be written as a vector form $\beta = [a_2 \ \cdots \ a_{Q-1} \ a_Q]^T_{Q-1}$. Based on (15)–(18), we have the following equations:

$$\zeta^{(g)} = \mathbf{M} \cdot \beta \quad (19)$$

$$M = [\delta_{u,q}]_{U_g \times (Q-1)}, \delta_{u,q} = q \cdot (q-1) \cdot \left(\alpha^{(g)}[u] \right)^{q-2}. \quad (20)$$

The least square error estimation of β can be obtained straightforwardly

$$\hat{\beta} = (\mathbf{M}^T \mathbf{M})^{-1} \mathbf{M}^T \zeta^{(g)}. \quad (21)$$

In order to ensure the existence of the inverse of $(\mathbf{M}^T\mathbf{M})$, a necessary condition is $U_g \geq Q$. In reality, after coarse motion compensation with navigation system, the motion error is with low frequency characteristics, and fifth-order polynomial assumption usually satisfies most real scenarios [7]. Then, the phase error function can be constructed by $\hat{\beta}$ for each SA range-compressed phase history $h_u^{(g)}(r_u^{(g)}, t_u^{(g)})$. Fourier transform is followed up to transform them back into focused SA images. Furthermore, by the phase corrected SA images, the FFBP recursion continues. In the next recursion, MAMD is performed to achieve better focal quality. The autofocus scheme is illustrated in Fig. 2.

In the first FFBP recursions, there are excessive SA images with low resolution. In this case, we can design a high-order polynomial model for the phase error, which would fit some high-frequency errors optimally. However, due to the shortness of sub-apertures, the precision of MD is limited and subsequently leads to low accuracy in the polynomial coefficients estimation. In contrast, when short SA images are fused into high-resolution ones during the FFBP recursion, precise Doppler rate estimate is achievable as aperture length is increased. However, due to the decrease of amount of SA images, only low-order polynomial phase model is applicable as discussed in (21). Taking amount and length of sub-apertures into account, we apply the scheme that the polynomial order decreases as the recursion amount increases. For example, when the length of sub-aperture is increased up to 16 in FFBP recursion, we begin the autofocus processing with polynomial order 8, and then, the order is decreased by one as recursion number increases every time until the polynomial order is equal to 4. In this scheme, the precision of instantaneous Doppler rate estimate and phase error order are balanced: in the beginning recursions of FFBP, high-order phase error can be corrected moderately, enhancing the focusing quality of the fused images in the next recursions, and along with the improvement of estimation precision, the residual phase error is compensated in the ending recursions with high accuracy. One may notice that the autofocus processing is seamlessly embedded in the FFBP recursion, and instantaneous Doppler rate estimation in each recursion can be implemented in a parallelized way, which leverages high efficiency to the autofocus processing.

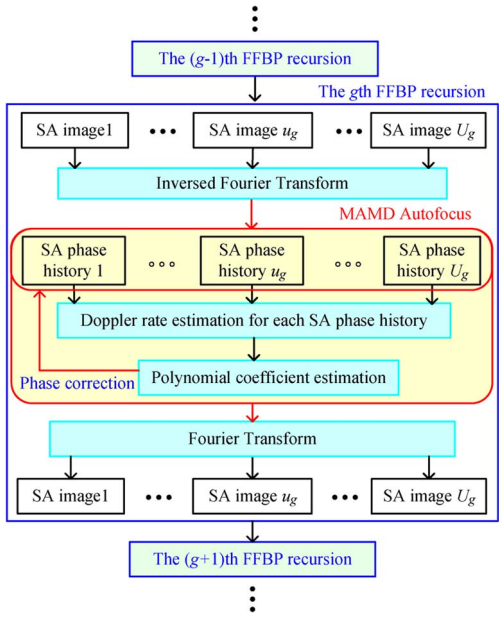

Fig. 2. FFBP with integration of MAMD autofocus.

IV. Real Data Experiments

In the following, through the analysis of raw high-resolution spotlight SAR data we want to investigate whether the phase error issue is adequately solved in FFBP imagery by integrating autofocus approaches. The test data set was collected by an X-band experimental SAR working at a spotlight mode. The pulse repetition frequency was 2,100 Hz, the synthetic aperture time was 15.6 seconds containing 16384 pulses, and the transmitting signal bandwidth was 1.16 GHz. The closest operating range to reference point was 10.5 km. The slant range image is 2 × 1 km in range and azimuth directions with a nominal range and azimuth resolutions of 0.15 × 0.15 m. By both original FFBP and FFBP integrating with MAMD to process the raw data, we may produce high-resolution and wide-swath SAR imageries. With blending the proposed MAMD approach, the motion error is achieved within the FFBP. Comparisons of imageries by the original FFBP and FFBP integrated with autofocus approaches are presented in Fig. 3. Due to the existence

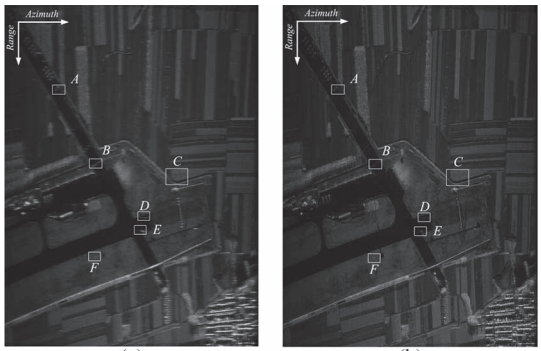

Fig. 3. FFBP images. (a) FFBP image without autofocus processing. (b) FFBP image with combining MAMD.

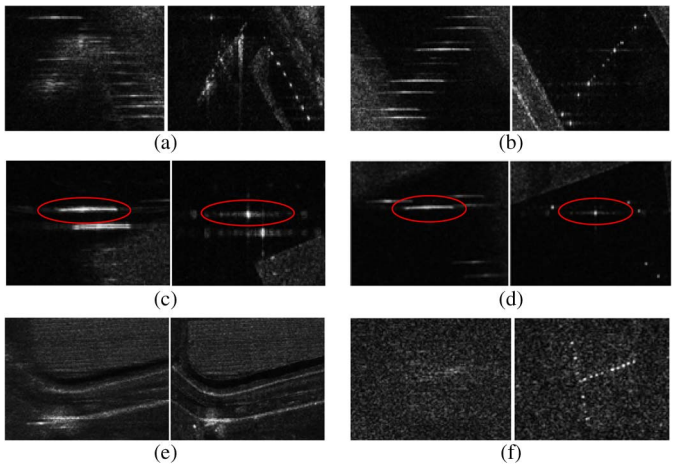

Fig. 4. Sub-scene images selected in Fig. 3.

of phase error, the FFBP image without autofocus processing involves in serious blurs as shown in Fig. 3(a), while the image obtained by the FFBP with embedding autofocus processing are well-focused over the whole scene as given in Fig. 3(b). Various types of targets, such as runway (dark signature near the middle), farmland, and urban areas (near bottom right corner) are shown in a clear way. Sub-scenes A–F in the imaging swath are magnified to assess the performance evaluation of the algorithms. Their magnified illuminations are shown in Fig. 4 for comparison. In each pair of sub-scenes image of Fig. 4, the left blurred image is achieved by directly applying FFBP, while the right one is obtained by the proposed approach.

From Fig. 4, we note that all sub-scene images generated by the proposed approach are well-focused, the point scatters are concentrated, and texture of some farmland is clear. In particular, sub-scenes C, D contain some close-located trihedral corner reflectors, and there is also a corner reflector array aligned in a "T" form in F. Compared to the results from original FFBP, those from FFBP combining with MAMD are focused precisely. All corner reflectors are identified clearly. In sub-scene C, there are two closed-located corner reflectors, with 0.15 meter distance in azimuth, which are circled in Fig. 4. To demonstrate the optimal performance of the proposed approach, we give their azimuth response in Fig. 5, where one can clearly find that by the proposed approach, the two reflectors are separated distinctively, which ensures the success of the proposed MAMD method. Through analysis, the effectiveness of FFBP integrating with MAMD is effective and satisfactory

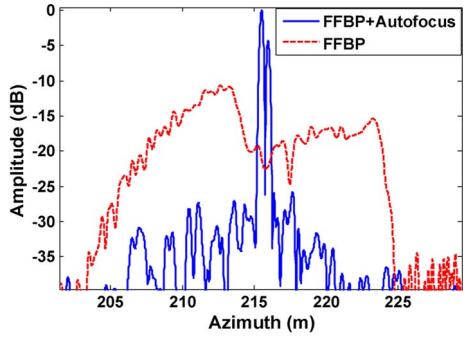

Fig. 5. Comparison of azimuth response of a corner pair circled in C.

to focus high-resolution spotlight SAR raw data with unknown phase errors.

V. Conclusion

In this letter, we blend a novel MAMD algorithm with FFBP for high-resolution spotlight SAR imagery. In our algorithm, a pseudo polar coordinate for SA image is suggested to develop the Fourier transform relationship between the SA image and its corresponding range-compressed phase history. As a result, the phase error function is estimated by the proposed MAMD. The MAMD is consistently embedded into the recursion of FFBP and furnishes FFBP with the capability of focusing raw data with motion error at high precision and efficiency. Real high-resolution spotlight SAR data experiments validate the effectiveness of our proposed approach.

References

[1] A. F. Yegulalp, "Fast backprojection algorithm for synthetic aperture radar," in *Proc. Radar Conf.*, Waltham, MA, USA, Apr. 20–22, 1999, pp. 60–65.

[2] L. M. H. Ulander, H. Hellsten, and G. Stenström, "Synthetic aperture radar processing using fast factorized back-projection," *IEEE Trans. Aerosp. Electron. Syst.*, vol. 39, no. 3, pp. 760–776, Jul. 2003.

[3] D. E. Wahl, D. A. Yocky, and C. V. Jakowatz, Jr., "An implementation of a fast backprojection image formation algorithm for spotlight-mode SAR," in *Proc. SPIE*, 2008, vol. 6970, pp. 69 700H–69 700H-11.

[4] C. V. Jakowatz and D. E. Wahl, "Considerations for autofocus of spotlight-mode SAR imagery created using a beamforming algorithm," in *Proc. SPIE—Algorithms Synthetic Aperture Radar Imagery XVI*, 2009, vol. 7337, pp. 73 370A-1–73 370A-9.

[5] M. Rodriguez-cassola, P. Parts, G. Krieger, and A. Moreira, "Efficient time-domain image formation with precise topography accommodation for general bistatic SAR configurations," *IEEE Trans. Aerosp. Electron. Syst.*, vol. 47, no. 4, pp. 2949–2966, Oct. 2011.

[6] K. A. C. de Macedo, R. Scheiber, and A. Moreira, "An autofocus approach for residual motion errors with application to airborne repeat-pass SAR interferometry," *IEEE Trans. Geosci. Remote Sens.*, vol. 46, no. 10, pp. 3151–3162, Oct. 2008.

[7] M. Xing, X. Jiang, R. Wu, F. Zhou, and Z. Bao, "Motion compensation for UAV SAR based on raw radar data," *IEEE Trans. Geosci. Remote Sens.*, vol. 47, no. 8, pp. 2870–2883, Aug. 2009.

[8] W. G. Carrara, R. S. Goodman, and R. M. Majewski, *Spotlight Synthetic Aperture Radar: Signal Processing Algorithm*. Boston, MA, USA: Artech House, 1995, pp. 245–254.

[9] H. Hellsten, L. M. Ulander, A. Gustavsson, and B. Larsson, "Development of VHF CARABAS II SAR," in *Proc. Radar Sens. Technol., SPIE AeroSense Conf.*, Orlando, FL, USA, 1996, pp. 48–60.

[10] V. T. Vu, T. K. Sjögren, M. I. Pettersson, and H. Hellsten, "An impulse response function for evaluation of UWB SAR imaging," *IEEE Trans. Signal Process.*, vol. 58, no. 7, pp. 3927–3932, Jul. 2010.

[11] G. Fornaro, G. Franceschetti, and S. Perna, "On center-beam approximation in SAR motion compensation," *IEEE Geosci. Remote Sens. Lett.*, vol. 3, no. 2, pp. 276–280, Apr. 2006.

[12] I. Cumming and F. Wang, *Digital Processing of Synthetic Aperture Radar Data: Algorithm and Implementation*. Norwood, MA, USA: Artech House, 2005.